Tropospheric Delay Calibration System performance during the first two BepiColombo solar conjunctions

Riccardo Lasagni Manghi[1], David Bernacchia[1], Luis Gomez Casajus[2], Marco Zannoni[1,2], Paolo Tortora[1,2], Antonio Martellucci[3], Javier De Vicente[4], Jose Villalvilla[4], Gerrit Maschwitz[5], Paolo Cappuccio[6], and Luciano Iess[6]

[1]Alma Mater Studiorum - Università di Bologna, Dipartimento di Ingegneria Industriale, Forlì, Italy.
[2]Alma Mater Studiorum - Università di Bologna, Centro Interdipartimentale di Ricerca Industriale Aerospaziale, Forlì, Italy.
[3]European Space Agency, ESA-ESTEC, Noordwijk, Netherlands.
[4]European Space Agency, ESA-ESOC, Darmstadt, Germany.
[5]RPG Radiometer physics GmbH, Meckenheim, Germany.
[6]Sapienza University of Rome, Department of Mechanical and Aerospace Engineering, Rome, Italy.

Corresponding author: Riccardo Lasagni Manghi (riccardo.lasagni@unibo.it)

Key Points:

- The Tropospheric Delay Calibration System installed at the Malargüe ground station was operated during the BepiColombo solar conjunctions.
- The system calibrations improved the Doppler measurements by 51% on average and up to 73% in optimal conditions.
- Calibrated two-way Doppler residuals satisfy the Mercury Orbiter Radioscience Experiment stability requirements.

Abstract

Media propagation delay and delay-rate induced by the water vapor within the Earth's troposphere represent one of the main error sources for radiometric measurements in deep space. In preparation for the BepiColombo and JUICE missions, the European Space Agency has installed the prototype of a tropospheric delay calibration system (TDCS) at the DSA-3 ground station located in Malargüe, Argentina. An initial characterization of the TDCS performance was realized using the orbit determination of the Gaia spacecraft as a testbed. This work will further characterize the system by analyzing the BepiColombo tracking passes, which were recorded between March 2021 and February 2022 during the first two superior solar conjunction experiments. The performance exceeds the expectations based on the previous analysis, with an average 51% reduction of the Doppler noise when using the TDCS measurements in place of standard calibrations based on global navigation satellite system data. The tropospheric instability at long time scales is also significantly reduced, with most of the tracking passes now satisfying the Mercury orbiter radioscience experiment (MORE) requirements on two-way Doppler stability.

1 Introduction

Radioscience experiments in recent deep space missions like Cassini, Juno, and BepiColombo, have reached very high standards in terms of accuracy and reliability thanks to the very precise radio tracking systems installed on the probes and on the ground. This high level of precision can be reached through the combination of X- and Ka-band communication links for both uplink and downlink, thanks to the simultaneous usage of two on-board transponders (Iess, et al., 2009), (Serra, et al., 2019), (Bertotti, et al., 1993). The linear combination of radiometric observables obtained through multi-frequency links allows to remove dispersive media propagation errors caused by the solar and interplanetary plasma and the Earth's ionosphere, which represent two of the largest noise sources in radio tracking. This improvement in radio systems' technology consequently led to increasingly demanding requirements in order to obtain higher accuracy during the orbit determination process.

For instance, the Mercury orbiter radioscience experiment (MORE) onboard BepiColombo, which will perform analyses in gravity science, geodesy and fundamental physics (Iess, et al., 2021), has a Doppler stability requirement, expressed in terms of Allan deviation, of $1.4 \cdot 10^{-14}$ for integration times larger than 1000 s, corresponding to an accuracy in range rate of about 0.004 mm/s (di Stefano, et al., 2021). At the same time, the availability of an onboard Ka-band transponder (KaT) enables precise pseudo-noise ranging measurements that have proven to reach an accuracy of less than 1 cm during tests performed on inflight data (Cappuccio, et al., 2020).

As a consequence, the focus has recently shifted towards the removal of non-dispersive error sources such as the ones due to the ground station hardware or the Earth's troposphere, which represent the highest noise contributors after the plasma-noise removal (Iess, et al., 2012).

In preparation for the BepiColombo and Juice missions, the European Space Agency has installed and operates the prototype of a new Tropospheric Delay Calibration System (TDCS) at the DSA-3 deep space ground station in Malargüe. This system, which is based on a high stability microwave radiometer, uses sky brightness temperature measurements at Ka- (~30 GHz) and V-bands (~60 GHz) to retrieve the path delay induced by water vapor along the instrument's line of sight, using a neural network retrieval algorithm specifically trained for the Malargüe site. The initial system qualification tests have already proven that using the TDCS calibrations in place of standard calibrations for the orbit determination of Gaia can significantly improve the quality of the radiometric measurements at X-band, with an average noise reduction of roughly 34% for the Doppler at 60 s count time (Lasagni Manghi, et al., 2021).

In this paper, we will further characterize the TDCS performance by analyzing the BepiColombo tracking passes that were recorded during the cruise phase as part of the solar conjunction experiments (SCE). The availability of a multi-frequency link for both Doppler and range measurements makes the BepiColombo mission a perfect testbed for addressing the contribution of tropospheric calibrations to the overall data quality.

In the following sections, 31 tracking passes recorded from the Malargüe ground station between March 2021 and February 2022 are analyzed as part of an orbit determination process. The noise characteristics of the range and Doppler measurement residuals obtained using the TDCS tropospheric calibrations are compared to those obtained using standard calibrations based on global navigation satellite system (GNSS) data. Finally, the noise characteristics are compared with the MORE requirements to verify the end-to-end system compliance.

2 Tropospheric Delay Calibration System

The TDCS is a prototype instrument for the estimation of the tropospheric delay and delay-rate along the line of sight of a deep space antenna. Its main subsystem is represented by a high-stability microwave radiometer, which measures the sky noise emissions at 14 frequency channels near the water vapor absorption line at 22.2 GHz, the oxygen absorption band around 60 GHz, and in the 30 GHz window that is mainly sensitive to liquid water content. This prototype includes a modified version of the HATPRO-G5 model developed by Radiometer physics GmbH (RPG), an external parabolic reflector to reduce the antenna beam width, an open-loop antenna control system for tracking passes of deep space missions, and a meteorological station. The TDCS includes a dew blower/heater system to remove water condensation from the exposed surfaces of the antenna system. It is completed by new calibration and tracking procedures, and software tools specifically developed for monitoring, automatic control, and commanding by the ground station systems. More details on the system are provided by Lasagni Manghi, et al. (2021) that used a similar setup for the orbit determination of the Gaia spacecraft.

3 Testbed summary and data availability

Table 1 provides an overview of the 31 BepiColombo tracking passes that were analyzed during this study and of the atmospheric conditions which were encountered during each pass. The first 17 passes are related to the first solar conjunction experiment (SCE1), which occurred between 10 March and 26 March 2021, corresponding to the local autumn in Malargüe. During these passes, the round-trip light time (RTLT) ranged from 1501 s at the beginning of March to 1518 s at the end. At the same time, the maximum elevation ranged from 60° to 51°, with only a few passes going below 20°.

The remaining 14 passes are related to the second solar conjunction experiment (SCE2), which occurred between 29 January and 12 February 2022, corresponding to the local summer. Here, the round-trip light time ranged from 1471 s in late January to 1330 s in early February. The elevation was more favorable with respect to SCE1, with maximum values ranging from 75° to 67° and no pass going below 25°.

Both solar conjunctions are characterized by extremely low values of elongation, with local minima of 1.2° and 2.1° occurring on 17 March 2021 and 4 February 2022, respectively. For tracking passes characterized by elongation values smaller than 3° the so called *Sun avoidance* mode was used, which consists in applying an offset between the TDCS pointing direction and the one of the deep space antenna to avoid the intrusion of solar radiation in the TDCS beamwidth. The side effect of this procedure is the progressive divergence between the air volumes observed by the TDCS and by the deep space antenna as the pointing offset increases. Among the atmospheric parameters shown in Table 1, the range of TDCS-retrieved zenith wet delay (ZWD) measurements provides an indication of the potential improvement that can be obtained when tropospheric calibrations are introduced in the orbit determination process. Values of the TDCS-retrieved liquid water path (LWP) above ~10 g/m^2 indicate the presence of condensed water (clouds or fog) along the instrument line-of-sight. This quantity scales with the length of the propagation path through the cloud. Therefore, values of LWP > 500-1000 g/m^2 (mapped to zenith), characteristic of thick cloud formations, may suggest the presence of rain within the sampled air volume. This information is complemented by the ground rain rate (RR) data measured close to the deep space antenna. Both these parameters are used for data quality assessment and to identify periods of adverse weather conditions for the TDCS calibrations. This is because the presence of clouds, rain, and horizontal atmospheric inhomogeneities along the slant-path can affect the accuracy of the retrieval algorithm, especially at low elevations.

Lastly, the wind speed (WS) at ground level provides a twofold indication: on one side it indicates the strength of the vibrations induced on the TDCS mechanical structure, which represent an additional noise source for the calibrated data; on the other side, it represents a proxy for the presence of turbulent eddies in the lower portions of the atmosphere, which affect the accuracy of the TDCS calibrations (Lasagni Manghi, et al., 2019).

Table 1 Summary of data availability and main meteorological parameters for the analyzed tracking passes. The columns indicate respectively the: 1) year; 2) day of the year (DOY); 3) calendar date; 4) time coverage; 5) characteristic elevation values (start of session, peak value, end of session); 6) 99th percentile of the retrieved liquid water path along the slant direction; 7) range of retrieved zenith wet delay values; 8) 99th percentile of the wind speed measured by the TDCS meteo station; 9) 99th percentile of the instantaneous rain rate measured by the TDCS meteo station; 10) average rain rate during the pass (integral of the instantaneous rain rate divided by the pass duration); 11) maximum pointing offset between the deep space antenna and the TDCS when in *Sun avoidance* mode.

Notes: (*) reduced portions of these passes were analyzed due to the adverse weather conditions. Specifically, we removed all data when one of the following conditions was met: a) rain was detected by TDCS meteo station, b) the dew blower was active, c) liquid water path along the slant direction was above 2000 g/m2; (†) data collected at elevations lower than 15° were removed during the data pre-processing; (‡) the Ka transponder lost the lock on the range in sporadic events, likely as a result of bad weather conditions at the station.

Year	DOY	Date	From/To	Elevation [°]	LWP [g/m^2]	ZWD [mm]	WS [km/h]	RR [mm/h]	RR_{pass} [mm/h]	Pointing offset [°]
2021	69	10 Mar	[12:45, 21:00]	[31, 61, 23]	56	[36, 58]	48	-	-	-
	70	11 Mar	[12:37, 20:50]	[28, 60, 25]	39	[60, 86]	26	-	-	-
	71	12 Mar	[12:38, 21:00]	[28, 60, 23]	54	[93, 135]	16	-	-	-
	72	13 Mar	[12:50, 21:00]*	[29, 59, 23]	6722	[89, 209]	19	38	2.13	0.03
	73	14 Mar	[12:38, 21:00]	[27, 59, 23]	1203	[99, 149]	17	-	-	0.65
	74	15 Mar	[12:50, 21:00]	[29, 59, 23]	521	[86, 148]	13	1	0.03	1.18
	75	16 Mar	[12:45, 21:00]	[27, 59, 23]	323	[63, 102]	19	-	-	1.64
	76	17 Mar	[12:50, 21:00]*	[27, 58, 24]	2194	[89, 129]	24	5	0.28	1.85
	77	18 Mar	[12:50, 21:00]	[25, 57, 25]	1022	[71, 94]	13	-	-	1.81
	78	19 Mar	[12:40, 21:00]	[22, 56, 24]	50	[47, 83]	13	-	-	1.52
	79	20 Mar	[16:32, 21:00]	[54, 55, 24]	37	[45, 66]	21	-	-	1.04
	80	21 Mar	[12:45, 21:00]	[23, 54, 23]	465	[75, 105]	19	-	-	0.48
	81	22 Mar	[12:45, 21:00]	[21, 53, 23]	51	[68, 86]	14	-	-	-
	82	23 Mar	[13:33, 21:14]	[29, 52, 20]	59	[41, 77]	14	1	0.03	-
	83	24 Mar	[12:45, 21:00]	[19, 52, 23]	178	[79, 114]	21	-	-	-
	84	25 Mar	[12:00, 20:20]*	[10, 51, 30]†	3032	[91, 156]	24	28	1.16	-
	85	26 Mar	[12:05, 20:19]	[10, 50, 30]†	888	[49, 74]	21	-	-	-
2022	29	29 Jan	[12:42, 21:00]	[39, 75, 31]	187	[32, 118]	31	-	-	-
	30	30 Jan	[12:42, 21:00]	[37, 75, 31]	29	[23, 59]	46	-	-	-

31	31 Jan	[12:47, 21:00]	[37, 74, 32]	33	[42, 74]	19	-	-	-
32	1 Feb	[12:51, 21:00]	[37, 74, 32]	45	[70, 120]	17	-	-	-
33	2 Feb	[12:40, 21:00]	[34, 74, 33]	484	[88, 135]	16	-	-	0.42
34	3 Feb‡	[12:40, 21:00]*	[33, 74 33]	2168	[90, 217]	21	12	0.45	0.76
35	4 Feb‡	[12:40, 21:00]	[32, 73, 34]	393	[56, 112]	36	-	-	0.93
36	5 Feb	[12:39, 21:00]	[31, 73, 34]	1029	[83, 123]	16	-	-	0.92
37	6 Feb	[12:40, 21:00]	[30, 72, 34]	32	[64, 109]	19	-	-	0.69
39	8 Feb	[12:39, 21:00]	[28, 70, 34]	33	[74, 113]	18	-	-	-
40	9 Feb	[12:46, 21:00]	[28, 69, 35]	34	[78, 101]	23	-	-	-
41	10 Feb	[12:45, 21:00]	[29, 69, 35]	441	[63, 121]	30	-	-	-
42	11 Feb	[12:45, 21:00]	[26, 68, 35]	196	[61, 87]	20	-	-	-
43	12 Feb	[12:38, 21:00]	[25, 67, 36]	116	[46, 61]	20	-	-	-

4 Orbit Determination analysis

4.1 Introduction

With the arrival in its final orbit scheduled for March 2026, the Mercury planetary orbiter (MPO) will perform the most precise radio science experiments ever conducted on Mercury. Before the orbital phase, the radio tracking system will be turned on, for experimental purposes, only concurrently with solar conjunctions to perform general relativity tests. A total of six solar conjunction experiments will be executed during the cruise phase: the presented work is based on the data collected during the first two conjunction experiments.

The analysis consists in performing side by side orbit determination processes using Doppler and ranging data collected during SCE1 and SCE2. The first orbit determination was performed applying GNSS-based calibrations, while the second was performed applying TDCS calibrations. The dynamical and observational models, the data pre-processing procedures, and the filter setup, were all maintained fixed between the two estimations in order to isolate the contribution of the tropospheric calibrations to the overall quality of the data.

4.2 Data selection and processing

The dataset comprised X- and Ka-band Doppler and range observables, collected at ESA's deep space ground station in Malargüe, which were delivered in TTCP format (Ricart, 2018). A first processing step consisted in removing the delay introduced by the electronic systems and by the antenna optical system of the ground station, which are measured during dedicated calibration sessions before and after the tracking passes. The second step consisted in removing the delays introduced by the spacecraft, which are obtained as a combination of calibration test results performed on ground and auto-calibration test results performed onboard before each pass (provided by the spacecraft telemetry). These delays are among the largest contributors to the noise of the range measurements, so their accurate calibration is of key importance to reduce the a priori uncertainty of the range biases, which are estimated for each tracking pass

Lastly, the data was reduced by removing all measurements collected at elevation angles lower than 15° and by manually discarding the outliers through a visual inspection of the Doppler and range residuals at 1 s count time.

4.3 Media calibrations

During periods of superior solar conjunction, the solar plasma becomes the highest contributor to the Doppler and range noises and is difficult to predict via analytical models due to short/medium scale variations of the electron density over the signal path (Verma, et al., 2013). To mitigate the effect of the solar plasma and of the Earth's ionosphere, the MPO uses a particular communication technique, called multi-frequency link, in which radiometric measurements at X/X, X/Ka, and Ka/Ka bands are linearly combined to remove the dispersive signal components (Bertotti, et al., 1993) (Mariotti & Tortora, 2013). This can be seen by expressing the range and Doppler observables for a coherent two-way link as the sum of a non-dispersive component z_{nd} and two components that scale with the uplink and downlink carrier frequencies, $f_\uparrow$ and $f_\downarrow$:

$$z = z_{nd} + \frac{P_\uparrow}{f_\uparrow^2} + \frac{P_\downarrow}{f_\downarrow^2} \tag{4.1}$$

In this expression, the coefficients $P_\uparrow$ and $P_\downarrow$ are proportional to the total electron content of the medium (electrons/m^2) for the range measurements and to its time derivative for the Doppler ones. Thanks to the multi-frequency link, three independent observables are acquired simultaneously by the ground station, namely z_{xx}, z_{xk}, and z_{kk}. By writing equation (4.1) for each of the observables we obtain a system of three equations in the three unknowns $P_\uparrow$, $P_\downarrow$, and z_{nd}. Solving for the non-dispersive term, which represents the plasma-free observable used in the subsequent analysis, we obtain the following expression:

$$z_{nd} = \left(\frac{1}{\beta^2 - 1}\frac{\alpha_{xx}^2}{\alpha_{kk}^2}\frac{\alpha_{xk}^2 - \alpha_{kk}^2}{\alpha_{xx}^2 - \alpha_{xk}^2}\right) z_{xx} + \left(\frac{1}{\beta^2 - 1}\frac{\alpha_{xk}^2}{\alpha_{kk}^2}\frac{\alpha_{kk}^2 - \alpha_{xx}^2}{\alpha_{xx}^2 - \alpha_{xk}^2}\right) z_{xk} + \left(\frac{\beta^2}{\beta^2 - 1}\right) z_{kk} \tag{4.2}$$

where $\alpha_{kk} = \frac{3360}{3599}$, $\alpha_{xk} = \frac{3344}{749}$, and $\alpha_{xx} = \frac{880}{749}$ are the turnaround ratios, and $\beta = \frac{f_{\uparrow k}}{f_{\uparrow x}}$ is the ratio between the X- and Ka- band uplink frequencies.

This method has been successfully applied to Cassini Doppler measurements in the past, showing a good stability in terms of Allan deviation at low elongations (Tortora, et al., 2004). However, for impact parameters of few solar radii ($b \lesssim 7R_\odot$) the noise cancellation scheme failed due to high density gradients in the corona (depending on solar activity) and to possible signal losses at X-band.

With the aim of validating the TDCS products, two different types of tropospheric calibrations were applied in separate orbit determination processes, whose results are then compared in the following sections:

a) Standard tropospheric calibrations, generated using dual-frequency GNSS measurements, were provided in the form of time-normalized polynomials of 6 h intervals according to the control statement processing (CSP) format described by JPL (2008);

b) TDCS calibrations were generated from measurements of atmospheric brightness temperature and concurrent meteorological data collected on site during the tracking passes, and according to the procedures described by Lasagni Manghi, et al. (2021). A neural network retrieval algorithm, trained for the site, was used to derive the slant wet delay along the spacecraft line of sight from the ground station antenna center, which was converted to zenith using analytical mapping functions. The zenith hydrostatic delay was derived from surface pressure measurements of the TDCS meteo station according to the model of Saastamoinen (1972) and scaled to the antenna's height. Both the wet and dry hydrostatic delays were written to CSP format using a piecewise linear fit with 20 s time intervals.

4.4 Dynamical model

The gravitational accelerations considered for this analysis included relativistic point-mass gravity for the Sun, the Solar System planets, and their satellites. Higher order spherical harmonics were included for Mercury and the Sun. The gravitational coefficients and state vectors of the different bodies were taken from JPL's DE438 planetary ephemerides.
Concerning non-gravitational accelerations, the largest contribution is given by the solar radiation pressure (SRP), which was computed using a standard flat plates model and assuming

a polyhedral shape for the main spacecraft components. Surface thermo-optical properties were considered to vary linearly between the launch and the end of mission.

Both of the analyzed solar conjunction experiments were characterized by the absence of thrusted maneuvers during the tracking intervals. Similarly, no reaction wheel desaturation maneuver was performed during the tracking intervals to preserve the coherency of the estimated spacecraft trajectories. Attitude data needed for the computation of the solar radiation pressure was retrieved from the operational SPICE kernel dataset (ESA SPICE service, DOI: 10.5270/esa-dwuc9bs).

4.5 Filter setup

The orbit determination was performed using the mission analysis, operations and navigation toolkit environment (MONTE) software developed by NASA's Jet Propulsion Laboratory (Evans, et al., 2018). This tool uses a weighted least-square batch filter, which minimizes the differences between the observed and the simulated measurements, also known as residuals, by adjusting the values of the dynamical and observational parameters shown in Table 2.

Specifically*, global* parameters are estimated once for the whole testbed campaign, while *local* parameters are estimated separately for each tracking pass. As a consequence, the estimated spacecraft trajectory is composed of separate trajectory arcs that can present discontinuities at the interval boundaries.

Table 2 Estimated parameters and their corresponding *a priori* knowledge.

Parameter	Type	N_{est}	*A priori σ*	*A priori value*
Spacecraft position	Local	$3\cdot N_{arcs}$	100 km	ESA Spice kernels
Spacecraft velocity	Local	$3\cdot N_{arcs}$	1 m/s	
SRP scale factor	Local	$1\cdot N_{arcs}$	1	1
Ground station range bias	Local	$1\cdot N_{arcs}$	1 km	0 km
S/C center of mass position (S/C body frame)	Global	3	10 cm	[0, 0, 0] m

5 Results

When the TDCS tropospheric calibrations are included within the orbit determination process, the radiometric measurements are affected by a variable amount of uncalibrated (or residual) tropospheric delay and by additional error sources, which are introduced by the calibrations. These sources include intrinsic errors, such as the thermal noise of the microwave radiometer receivers or the losses of the TDCS optical components, and scene-dependent errors induced by the atmospheric retrieval algorithm and by the mismatch between the air volumes contained in the antenna beams of the ground station and of the TDCS. Some of these individual contributions can be estimated through laboratory testing or simulations and were the subject of previous investigations by the authors (Maschwitz, et al., 2019), (Graziani, et al., 2014). However, predicting the overall tropospheric error on 2-way radiometric measurements from the individual error contributions is a challenging task, since most of these error sources are mutually correlated and depend on atmospheric variables which can be difficult to assess, like the amount of tropospheric turbulence contained in the antenna beam.

For the current analysis we opted for an end-to-end approach, which consists in directly evaluating the statistics of the Doppler and range residuals and comparing them to the system requirements. After a careful calibration of the dispersive noise sources, using the multi-frequency link described above (section 4.3), and of the of measurement biases, the processed radiometric measurements result to be mostly affected by mechanical noise and residual tropospheric errors. An initial assessment of the TDCS calibration quality is obtained by computing the root mean square (rms) value of the Doppler residuals at 60 s count time for

each tracking pass and by comparing its value with the one obtained using standard GNSS calibrations.
The count time value of 60 s was selected since it is sufficiently smaller than the characteristic time scales of the typical investigated processes and sufficiently large to avoid numerical noise issues (Zannoni & Tortora, 2013), thus representing a standard case for radioscience applications (Gomez Casajus, et al., 2021), (Durante, et al., 2019), (Zannoni, et al., 2020), (Tortora, et al., 2016). Similarly, the calibration quality on range measurements is evaluated by comparing the rms values of the residuals at sampling intervals of 1 s. This value corresponds to the one provided in the input TTCP files, although the real integration time coming from the ground station receiver configuration is 2 s.
A further assessment of the TDCS calibration quality is obtained by computing the overlapping Allan standard deviation (ASD) of the Doppler residuals at 1 s count time and comparing its value at characteristic time scales with the one obtained for standard GNSS calibrations.
In the following, the two solar conjunction experiments are treated separately to account for seasonal variations of the observing conditions (e.g. elevation profiles, air temperatures and water vapor content). A summary of the performances for the whole test campaign will then be given in Section 6.

5.1 Solar Conjunction Experiment 1

Figure 1 depicts the Doppler residuals at 60 s count time for SCE1. A comparison of the rms values for both Doppler and range residuals of individuals tracking passes is given in Table 3. An average Doppler noise reduction of 45% is observed when switching between the GNSS-based and TDCS calibrations, with only two passes showing reductions of less than 20% and a maximum reduction of 64% on 13 March. A more limited noise reduction of 1% is observed for the range, with a single tracking pass showing an increased rms value due to the introduction of some signatures at low frequencies. Furthermore, most of the tracking passes show a drop in the autocorrelation functions of both Doppler and range, indicating a whitening of the residuals. This effect is shown in Figure 2 for the test case of the March 15 pass, where we observe that the Doppler autocorrelation is non-zero only for short time delays and around the round-trip light time. This pattern, which is characteristic of two-way signals, indicates the presence of either mechanical noise or uncalibrated tropospheric errors, since the two effects are not distinguishable (Armstrong, et al., 2009).
It should be noted that the data recorded on 17 March was removed from the analysis due to the presence of rain for the majority of the tracking interval. Similarly, portions of the data were removed from the tracking passes of 13 March and 25 March, when rain was detected by the TDCS meteo station or the antenna blower system was turned on (indicating the presence of residual water on the optical surfaces). This is because we expect a degrading quality of the retrieved delay in both situations.

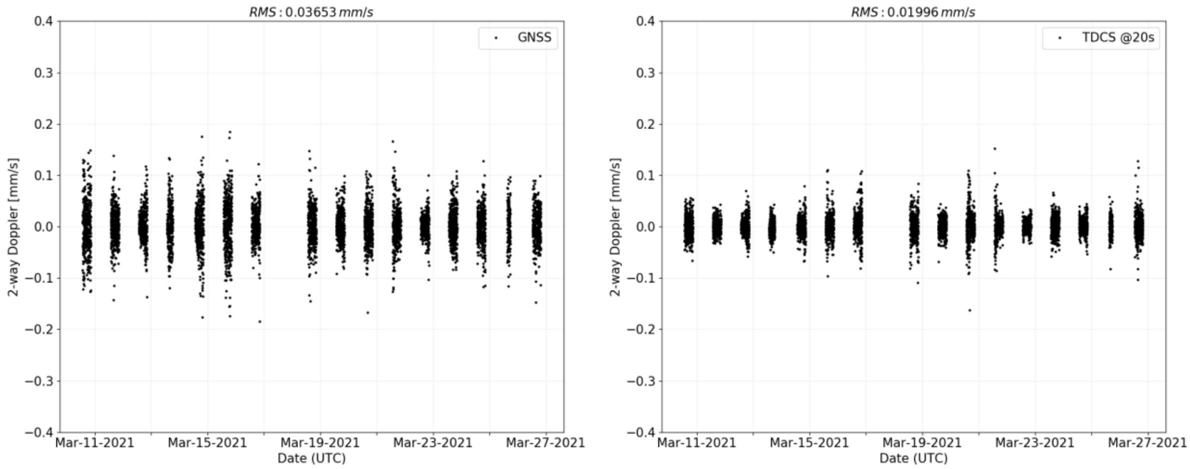

Figure 1 Comparison of the Doppler residuals at 60 s count time for SCE1. Left: using GNSS-based calibrations; right: using TDCS calibrations with 20 s integration time.

Figure 3 depicts the Allan deviation of the Doppler residuals at 1 s count time for the individual tracking passes. The black dashed line represents the MORE requirement for 2-way Doppler residuals, corresponding to a maximum ASD value of $1.4 \cdot 10^{-14}$ at integration times $\tau > 1000$ s. This requirement was then mapped to shorter stability intervals using the expression for white noise $ASD(\tau) = ASD(\tau_{req})\sqrt{\tau_{req}/\tau}$, which is well approximating the behavior observed at typical time scales of interest for radioscience observations (e.g. 1-10000 s). We can see that the stability requirement is satisfied for most of the tracking passes when using the TDCS calibrations, with the exception of the ones of 16 March and 20 March.

Lastly, Figure 4 summarizes the ASD values for both scenarios at time intervals which are typical for radioscience applications, namely 20 s, 60 s, and 1000 s. We can observe a consistent improvement for all tracking passes, with the highest reductions being obtained for longer time intervals. However, the stability improvement is less pronounced for the tracking passes characterized by low elongation values due to the pointing offset introduced by the *Sun avoidance* mode.

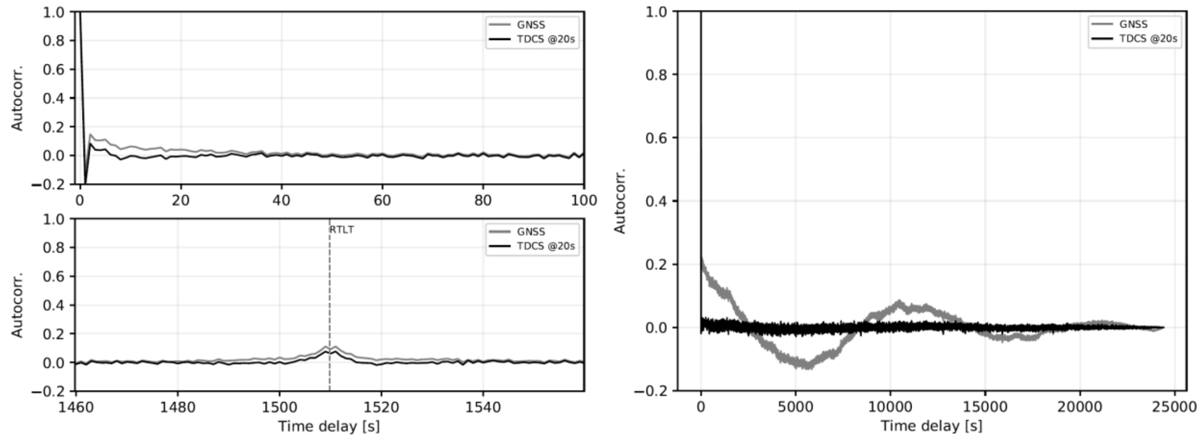

Figure 2 Autocorrelation of the residuals for the pass of 15 March. Left: Doppler residuals at 1 s count time. The upper plot shows a zoom at short time delays, while the lower plot shows a zoom around the round-trip light time (RTLT≈1510 s, dashed line); right: range residuals.

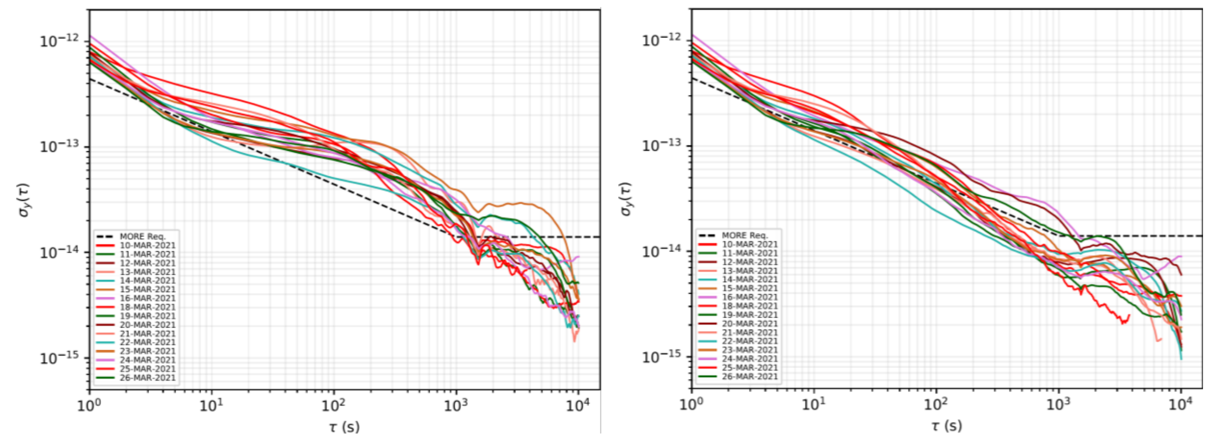

Figure 3 Allan deviation of the Doppler residuals at 1 s count time for SCE1. Left: using GNSS-based calibrations; right: using TDCS calibrations with 20 s integration time.

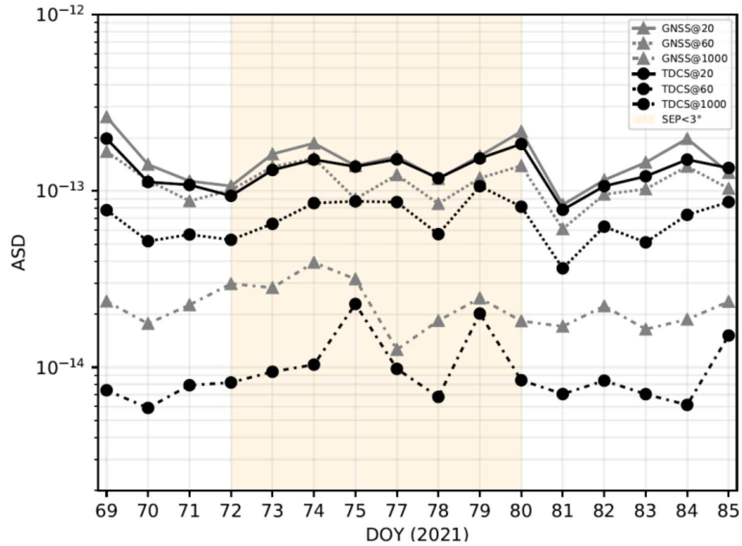

Figure 4 Comparison of the ASD values of the Doppler residuals at 1 s count time for SCE1 derived from GNSS (▲) and TDCS (●) data; ASD values are displayed at characteristic stability intervals of 20 s (solid line), 60 s (dotted line), and 1000 s (dash-dotted line). The shaded area marks the tracking passes for which the *Sun avoidance* mode is active (SEP angle < 3°)

Table 3 Rms values of the Doppler and range residuals for individual tracking passes of SCE1. The Doppler count time is T_C = 60 s; the range sampling interval is T_S = 1 s, while the true ground station integration time is T_{GS} = 2 s.

DOY	**Date**	**Rms of Doppler res. [µm/s] (full link, T_C = 60 s)**			**Rms of range res. [cm] (full link, T_S = 1 s, T_{GS} = 2 s)**		
		GNSS	**TDCS**	**Ratio**	**GNSS**	**TDCS**	**Ratio**
69	10 Mar	49.91	20.59	0.41	4.31	4.27	0.99
70	11 Mar	33.30	12.98	0.39	2.97	2.98	1.00
71	12 Mar	29.97	16.94	0.57	2.99	2.99	1.00
72	13 Mar	41.44	15.05	0.36	3.05	3.03	0.99
73	14 Mar	44.67	17.21	0.39	3.17	3.09	0.97
74	15 Mar	50.98	22.90	0.45	3.29	2.94	0.89
75	16 Mar	31.05	25.85	0.83	3.15	3.16	1.00
77	18 Mar	35.40	23.32	0.66	3.08	3.07	1.00
78	19 Mar	28.28	15.44	0.55	2.93	2.89	0.98
79	20 Mar	35.79	30.01	0.84	2.88	2.91	1.01
80	21 Mar	38.01	22.28	0.59	2.87	2.85	0.99
81	22 Mar	20.21	10.92	0.54	2.89	2.87	0.99
82	23 Mar	32.63	18.16	0.56	2.91	2.88	0.99
83	24 Mar	31.44	13.34	0.42	2.89	2.88	0.99
84	25 Mar	39.89	19.35	0.49	2.91	2.90	0.99
85	26 Mar	32.84	23.44	0.71	2.91	2.85	0.98
Average		**35.99**	**19.24**	**0.55**	**3.08**	**3.03**	**0.99**

95th Percentile	**50.18**	**26.89**	**0.83**	**3.54**	**3.43**	**1.01**

5.2 Solar Conjunction Experiment 2

Figure 5 depicts the Doppler residuals at 60 s count time for SCE2. Rms values of both Doppler and range residuals for individuals tracking passes are then compared in Table 4.
An average Doppler noise reduction of 58% is observed when switching from standard calibrations to TDCS calibrations, with no pass showing reductions of less than 41% and a maximum reduction of 73% on 3 February. An average noise reduction of 3% is instead observed for the range, with two passes showing increased rms values. This significant boost in the calibration performances with respect to SCE1 is likely the result of two contributing factors: on one hand, tracking passes recorded during SCE2 in summer can be characterized by higher turbulence levels and water vapor contents with respect to the ones recorded during SCE1 in autumn, as indicated by the increased noise values for the GNSS scenario; on the other hand, lower noise levels are observed in the TDCS scenario as a result both of hardware and software updates, which were implemented in the time interval between the two experiments, namely an improvement of the control procedures for the antenna tracking and the adoption of a shorter duty cycle for the internal gain calibration of the TDCS microwave radiometer.

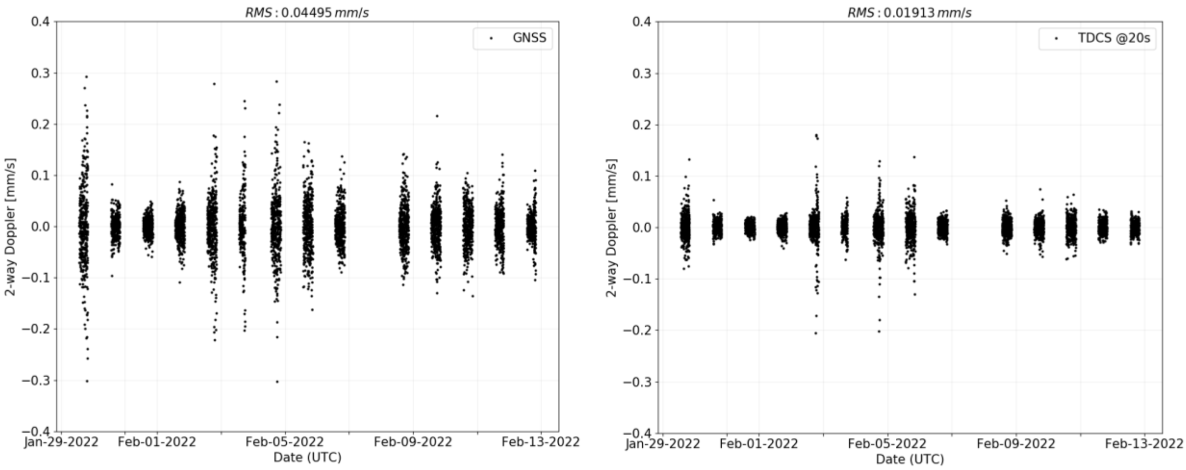

Figure 5 Comparison of the Doppler residuals at 60 s count time for SCE2. Right: using GNSS-based calibrations; left: using TDCS calibrations with 20 s integration time.

Figure 6 depicts the Allan deviation of the Doppler residuals at 1 s count time for the individual tracking passes of SCE2. As observed during SCE1, most of the tracking passes are consistent with the MORE requirements at stability intervals $\tau > 1000$ s when TDCS calibrations are used, with the exception of 2 February. Most of the tracking passes also show a drop in the autocorrelation function for both Doppler and range residuals, as indicated in Figure 7 for the test case of the 29 January 2022.
Finally, Figure 8 summarizes the Allan deviation at characteristic stability intervals. With respect to the previous case, we observe a more pronounced reduction of the ASD curves at short stability intervals and particularly at 20 s, while the reduction is more or less consistent at 1000 s. One noticeable exception is represented by the tracking pass of 12 February, where we observe a Doppler signature with characteristic timescales of a few hours, causing an increment in the ASD value at 1000 s. The cause of this signature, which is introduced by the TDCS calibrations, is currently under investigation and is expected to be related to a retrieval algorithm error. It should also be mentioned that the stability reduction observed for tracking passes during which the *Sun avoidance* mode is active is less pronounced with respect to SCE1. This is likely due to higher elongation values, corresponding to lower pointing offsets, and

higher elevation angles that reduce the volume mismatch between the TDCS and the deep space antenna beamwidths.

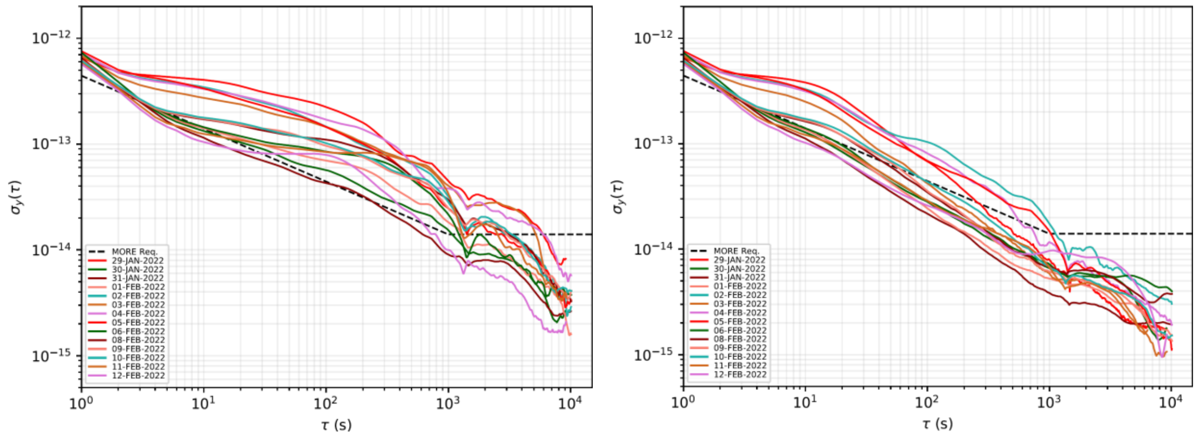

Figure 6 Allan deviation of the Doppler residuals at 1 s count time for SCE2. Left: using GNSS-based calibrations; right: using TDCS calibrations with 20 s integration time.

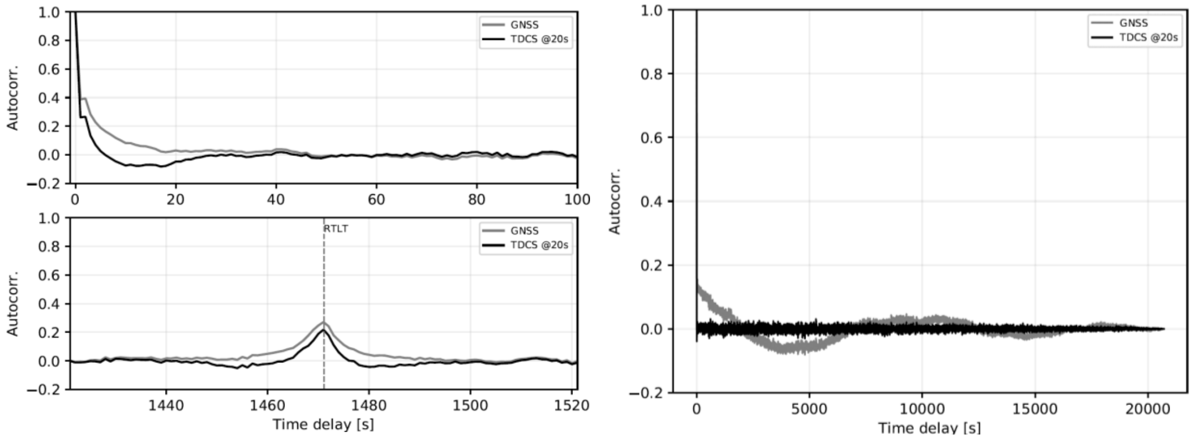

Figure 7 Autocorrelation of the residuals for the pass of 29 January 2022. Left: Doppler residuals at 1 s count time. The upper plot shows a zoom at short time delays, while the lower plot show a zoom around the round-trip light time (RTLT≈1472 s, dashed line); right: range residuals.

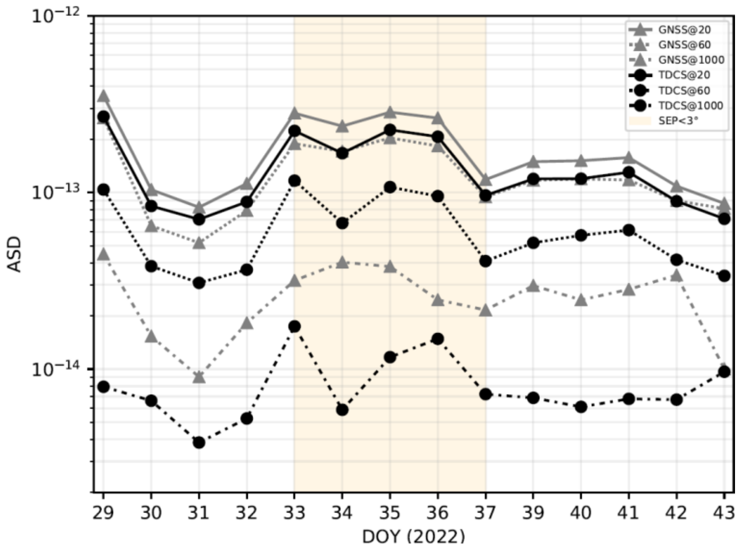

Figure 8 Comparison of the ASD values of the Doppler residuals at 1 s count time for SCE2 derived from GNSS (▲) and TDCS (●) data; ASD values are displayed at characteristic stability intervals of 20 s (solid line), 60 s (dotted line), and 1000 s (dash-dotted line). The shaded area marks the tracking passes for which the *Sun avoidance* mode is active (SEP angle < 3°).

Table 4 Rms values of the Doppler and range residuals for the individual tracking passes of SCE2. The Doppler count time is $T_C = 60$ s; the range sampling interval is $T_S = 1$ s, while the true ground station integration time is $T_{GS} = 2$ s.

DOY	Date	Rms of Doppler res. [μm/s] (full link, $T_C = 60$ s)			Rms of range res. [cm] (full link, $T_S = 1$ s, $T_{GS} = 2$ s)		
		GNSS	**TDCS**	**Ratio**	**GNSS**	**TDCS**	**Ratio**
29	29 Jan	80.52	25.09	0.31	3.15	2.87	0.91
30	30 Jan	20.87	10.72	0.51	2.80	2.77	0.99
31	31 Jan	15.68	8.00	0.51	2.87	2.87	1.00
32	01 Feb	26.12	10.13	0.39	2.98	3.00	1.01
33	02 Feb	56.68	33.62	0.59	2.91	2.83	0.97
34	03 Feb	58.37	15.93	0.27	3.24	2.96	0.92
35	04 Feb	64.34	30.12	0.47	3.03	2.83	0.93
36	05 Feb	52.74	28.50	0.54	2.98	2.91	0.98
37	06 Feb	33.08	10.79	0.33	2.75	2.76	1.00
39	08 Feb	40.93	13.91	0.34	2.63	2.62	1.00
40	09 Feb	38.42	14.10	0.37	2.92	2.82	0.97
41	10 Feb	37.93	17.17	0.45	2.69	2.63	0.98
42	11 Feb	35.06	11.05	0.32	2.48	2.42	0.97
43	12 Feb	25.40	10.62	0.42	2.54	2.57	1.01
Average		**41.87**	**17.12**	**0.42**	**2.85**	**2.78**	**0.97**
95th Percentile		**70.00**	**31.35**	**0.56**	**3.18**	**2.98**	**1.01**

6 Conclusions

This work focused on the characterization of the TDCS performance during the scheduled tracking passes for the first two solar conjunctions experiments to be carried out by the BepiColombo mission. The analysis consisted in a side-by-side comparison of Doppler and range residuals obtained when using alternatively GNSS-based or TDCS tropospheric calibrations as part of a multi-arc orbit determination process.

For the 16 tracking passes of SCE1, which occurred in March 2021 during the local autumn in Malargüe, we observed average Doppler noise reductions of 45%, with a maximum reduction of 64%. The 14 tracking passes of SCE2, which occurred between January and February 2022 during the local summer, marked a significant boost with respect to SCE1, with average Doppler noise reductions of 58% and a maximum reduction of 73%. These results are in line with the ones reported for the Juno gravity science investigations when using the Advanced Water Vapor Radiometer (AWVR) installed at the DSS-25 ground station in Goldstone, California (Buccino et al., 2021).

A significant improvement was also observed in the Doppler stability at all characteristic time scales, when using TDCS calibrations. As a result, the MORE stability requirement for two-way Doppler observables, which is expressed in terms of Allan deviation at 1000 s intervals, is satisfied for all tracking passes except three having extremely low elongation values.

Overall, the performance exceeded the expectations based on the previous analysis for the orbit determination of Gaia, which was used as a qualification testbed. A contributing factor to these improved results is represented by an increased power and variability of the sky noise measured by the TDCS. Higher water vapor content and turbulence strength are in fact observed during daytime hours (as opposed to the nighttime observations of Gaia), and particularly during the summer months of SCE2. At the same time, the use of a Ka-band transponder and a multi-frequency link allowed for the complete cancellation of the dispersive noise sources from the Earth's ionosphere and the solar plasma. Finally, a series of hardware and software updates were implemented in the time interval between the Gaia and BepiColombo test campaigns, as well as between the two solar conjunction experiments, which further contributed to the reduction of the residual tropospheric noise after the calibrations.

It should be noted that some portions of the tracking passes, during which atmospheric conditions unfavorable for retrieval were observed (e.g. in case of heavy rain), were removed from the orbit determination analysis due to the degradation of the retrieval algorithm

performance. The dataset of tracking passes involving the TDCS is currently too small to produce a robust statistical characterization of the retrieval accuracy as a function of the possible atmospheric conditions, however the current dataset shows that the use of TDCS permits a better calibration in particular during the local summer season when larger tropospheric turbulence and water vapor can occur. This is due to the capability of the TDCS to measure the delay introduced by the troposphere in the region illuminated by the deep space antenna beam with sampling rates higher than those of GNSS retrievals.
Future work will include observations from BepiColombo, Gaia, and other spacecraft routinely tracked from the Malargüe station, with the aim of producing an automatic filtering scheme for periods of low-quality data based on the observed atmospheric conditions.
Furthermore, a complete characterization of the range calibration performances (i.e. of the delay retrieval accuracy) will require switching from a multi-arc orbit determination approach to a single-arc approach with long integration times, and evaluating the variations of the range biases estimated during each tracking pass. This effort will require implementing higher-fidelity dynamical models for the BepiColombo non gravitational accelerations, to maintain the trajectory coherence between successive tracking passes.

Acknowledgments

R. Lasagni Manghi, M. Zannoni, P. Tortora wish to acknowledge Caltech and the Jet Propulsion Laboratory for granting the University of Bologna a license to an executable version of the MONTE project edition software.

Data Availability Statement:

Data used for this research will be made publicly available through the Guest Storage Facility (GSF) within ESA's Planetary Science Archive (https://www.cosmos.esa.int/web/psa/psa_gsf). This data set will include all raw measurements and ancillary information required for replicating the BepiColombo orbit determination analysis.

Funding:

The research described in this paper was carried out in the framework of ESA contract No. 4000116932/16/NL/AF “Development of a Ground Tropospheric Media Calibration System for Accurate Ranging of Space Science Missions”

7 References

Armstrong, J. W., Estabrook, F. B., Asmar, S. W., Iess, L., & Tortora, P. (2008). Reducing antenna mechanical noise in precision spacecraft tracking. Radio Science, 43(3). https://doi.org/10.1029/2007RS003766

Bertotti, B., Comoretto, G., & Iess, L. (1993). Doppler tracking of spacecraft with multi-frequency links. Astronomy and Astrophysics, 269, 608–616. Retrieved from https://ui.adsabs.harvard.edu/abs/1993A&A...269..608B

Buccino, D. R., Kahan, D. S., Parisi, M., Paik, M., Barbinis, E., Yang, O., et al. (2021). Performance of Earth Troposphere Calibration Measurements With the Advanced Water Vapor Radiometer for the Juno Gravity Science Investigation. Radio Science, 56(12). https://doi.org/10.1029/2021RS007387

Cappuccio, P., Notaro, V., di Ruscio, A., Iess, L., Genova, A., Durante, D., et al. (2020). Report on First Inflight Data of BepiColombo’s Mercury Orbiter Radio Science Experiment. IEEE Transactions on Aerospace and Electronic Systems, 56(6), 4984–4988. https://doi.org/10.1109/TAES.2020.3008577

Durante, D., Hemingway, D. J., Racioppa, P., Iess, L., & Stevenson, D. J. (2019). Titan's gravity field and interior structure after Cassini. Icarus, 326, 123–132. https://doi.org/10.1016/j.icarus.2019.03.003

ESA SPICE Service, BepiColombo Operational SPICE Kernel Dataset, https://doi.org/10.5270/esa-dwuc9bs

Evans, S., Taber, W., Drain, T., Smith, J., Wu, H.-C., Guevara, M., et al. (2018). MONTE: the next generation of mission design and navigation software. CEAS Space Journal, 10(1), 79–86. https://doi.org/10.1007/s12567-017-0171-7

Gomez Casajus, L., Zannoni, M., Modenini, D., Tortora, P., Nimmo, F., Van Hoolst, T., et al. (2021). Updated Europa gravity field and interior structure from a reanalysis of Galileo tracking data. Icarus, 358, 114187. https://doi.org/10.1016/j.icarus.2020.114187

Graziani, A., Jarlemark, P., Elgered, G., Martellucci, A., Mercolino, M., & Tortora, P. (2014). Assessment of Ground-Based Microwave Radiometry for Calibration of Atmospheric Variability in Spacecraft Tracking. IEEE Transactions on Antennas and Propagation, 62(5), 2634–2641. https://doi.org/10.1109/TAP.2014.2307582

Iess, L., Asmar, S., & Tortora, P. (2009). MORE: An advanced tracking experiment for the exploration of Mercury with the mission BepiColombo. Acta Astronautica, 65(5–6), 666–675. https://doi.org/10.1016/j.actaastro.2009.01.049

Iess, L., Budnik, F., Colamarino, C., Corbelli, A., Di Benedetto, M., Fabbri, V., et al. (2012). ASTRA: Interdisciplinary study on enhancement of the end-to-end accuracy for spacecraft tracking techniques. Proceedings of the International Astronautical Congress, IAC. 53425–3435.

Iess, L., Asmar, S. W., Cappuccio, P., Cascioli, G., De Marchi, F., di Stefano, I., et al. (2021). Gravity, Geodesy and Fundamental Physics with BepiColombo's MORE Investigation. Space Science Reviews, 217(1), 21. https://doi.org/10.1007/s11214-021-00800-3

JPL. (2008). TRK-2-23 Media Calibration Interface. 820-013. Deep Space Network (DSN), External Interface Specification, JPL D-16765, Revision C (draft). Retrieved from http://dawndata.igpp.ucla.edu/download.jsp?file=documents/Gravity/DATA_SET_DESCRIPTION/TRK-2-23_REVC_L5.PDF

Lasagni Manghi, R., Maschwitz, G., Tirtira, P., Rose, T., Martellucci, A., De Vicente, J., et al. (2019). Tropospheric delay calibration system (TDCS): Design and performances of a new generation of microwave radiometers for ESA deep space ground stations. TT&C workshop.

Lasagni Manghi, R., Zannoni, M., Tortora, P., Martellucci, A., De Vicente, J., Villalvilla, J., et al. (2021). Performance Characterization of ESA's Tropospheric Delay Calibration System for Advanced Radio Science Experiments. Radio Science, 56(10). https://doi.org/10.1029/2021RS007330

Mariotti, G., & Tortora, P. (2013). Experimental validation of a dual uplink multifrequency dispersive noise calibration scheme for Deep Space tracking: DUAL UPLINK INCOMPLETE LINK. Radio Science, 48(2), 111–117. https://doi.org/10.1002/rds.20024

Maschwitz, G., Czekala, H., Orlandi, E., & Rose, T. (2019). Accuracy and performance of atmospheric delay by a RPG microwave radiometer with respect to ground calibration systems for ESA radioscience. TT&C workshop.

Ricart, M. (2018). TTCP Software Interface Control Document (ICD) for RM datasets (Issue 2.1).

Saastamoinen, J. (2013). Atmospheric Correction for the Troposphere and Stratosphere in Radio Ranging Satellites. In S. W. Henriksen, A. Mancini, & B. H. Chovitz (Eds.), Geophysical Monograph Series (pp. 247–251). Washington, D. C.: American Geophysical Union. https://doi.org/10.1029/GM015p0247

Serra, D., Lari, G., Tommei, G., Durante, D., Gomez Casajus, L., Notaro, V., et al. (2019). A solution of Jupiter's gravitational field from Juno data with the orbit14 software. Monthly Notices of the Royal Astronomical Society, 490(1), 766–772. https://doi.org/10.1093/mnras/stz2657

di Stefano, I., Cappuccio, P., & Iess, L. (2021). The BepiColombo solar conjunction experiments revisited. Classical and Quantum Gravity, 38(5), 055002. https://doi.org/10.1088/1361-6382/abd301

Tortora, P., Iess, L., Bordi, J. J., Ekelund, J. E., & Roth, D. C. (2004). Precise Cassini Navigation During Solar Conjunctions Through Multifrequency Plasma Calibrations. Journal of Guidance, Control, and Dynamics, 27(2), 251–257. https://doi.org/10.2514/1.997

Tortora, Paolo, Zannoni, M., Hemingway, D., Nimmo, F., Jacobson, R. A., Iess, L., & Parisi, M. (2016). Rhea gravity field and interior modeling from Cassini data analysis. Icarus, 264, 264–273. https://doi.org/10.1016/j.icarus.2015.09.022

Verma, A. K., Fienga, A., Laskar, J., Issautier, K., Manche, H., & Gastineau, M. (2013). Electron density distribution and solar plasma correction of radio signals using MGS, MEX, and VEX spacecraft navigation data and its application to planetary ephemerides. Astronomy & Astrophysics, 550, A124. https://doi.org/10.1051/0004-6361/201219883

Zannoni, M., & Tortora, P. (2013). Numerical Error in Interplanetary Orbit Determination Software. Journal of Guidance, Control, and Dynamics, 36(4), 1008–1018. https://doi.org/10.2514/1.59294

Zannoni, M., Hemingway, D., Gomez Casajus, L., & Tortora, P. (2020). The gravity field and interior structure of Dione. Icarus, 345, 113713. https://doi.org/10.1016/j.icarus.2020.113713